Journal of Power Sources 627 (2025) 235848

Contents lists available at ScienceDirect

Journal of Power Sources

journal homepage: www.elsevier.com/locate/jpowsour

Redox-active a pyrene-4,5,9,10-tetraone and thienyltriazine-based conjugated microporous polymers for boosting faradaic supercapacitor energy storage

Swetha V. Chaganti [a,b], Santosh U. Sharma [a,b], Mervat Ibrahim [c], Abdul Basit [d], Poonam Nagendra Singh [d], Shiao-Wei Kuo [d,e,*], Mohamed Gamal Mohamed [d,f,**]

[a] Department of Chemistry, National Sun Yat-Sen University, Kaohsiung, 80424, Taiwan
[b] International PhD Program for Science, National Sun Yat-sen University, Kaohsiung, 80424, Taiwan
[c] Department of Chemistry, Faculty of Science, New Valley University, El-Kharja, 72511, Egypt
[d] Department of Materials and Optoelectronic Science, College of Semiconductor and Advanced Technology Research, Center for Functional Polymers and Supramolecular Materials, National Sun Yat-Sen University, Kaohsiung, 804, Taiwan
[e] Department of Medicinal and Applied Chemistry, Kaohsiung Medical University, Kaohsiung, 807, Taiwan
[f] Department of Chemistry, Faculty of Science, Assiut University, Assiut, 71515, Egypt

HIGHLIGHTS

- The redox-active TTh-Ph-PyTE CMP was synthesized via the Suzuki reaction.
- The TTh-Ph-PyTE CMP electrode reached a capacitance of 1041 F g^{-1} at 1 A g^{-1}.
- The capacitance of TTh-Ph-PyTE CMP in a symmetric device was 242 F g^{-1} at 1 A g^{-1}.

GRAPHICAL ABSTRACT

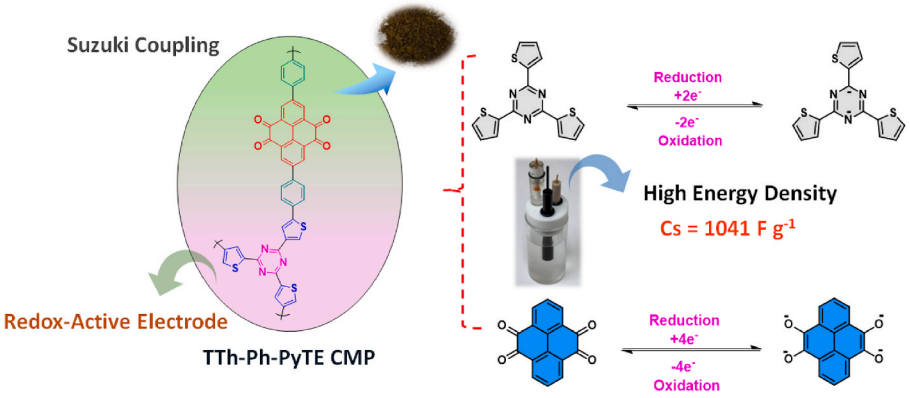

ARTICLE INFO

Keywords:
Redox-active units
Pyrene-4,5,9,10-tetraone
Thienyltriazine

ABSTRACT

Conventional supercapacitor electrodes typically suffer from drawbacks such as low energy density, short cycle life, and poor conductivity. In contrast, conjugated microporous polymers (CMPs) present a more advantageous option, providing higher surface area, greater cycle stability, and enhanced electrical properties. Utilizing pyrene-4,5,9,10-tetraone (PyTE) as a key redox-active component, we successfully prepare pyrene-4,5,9,10-

* Corresponding author. Department of Materials and Optoelectronic Science, College of Semiconductor and Advanced Technology Research, Center for Functional Polymers and Supramolecular Materials, National Sun Yat-Sen University, Kaohsiung, 804, Taiwan.
** Corresponding author. Department of Materials and Optoelectronic Science, College of Semiconductor and Advanced Technology Research, Center for Functional Polymers and Supramolecular Materials, National Sun Yat-Sen University, Kaohsiung, 804, Taiwan.
E-mail addresses: kuosw@faculty.nsysu.edu.tw (S.-W. Kuo), mgamal.eldin12@yahoo.com, mgamal.eldin12@aun.edu.eg (M.G. Mohamed).

https://doi.org/10.1016/j.jpowsour.2024.235848
Received 3 May 2024; Received in revised form 16 October 2024; Accepted 12 November 2024
Available online 21 November 2024

Conjugated microporous polymers
High specific capacitance

tetraone-thiophene polymer (PyTE-Th Polymer) and Thienyltriazine-pyrene-4,5,9,10-tetraone conjugated microporous polymer (TTh-Ph-PyTE CMP). This particular set of materials has been tailored for supercapacitor applications, employing a nitrogen-rich triazine, conductive thiophene (Th), and redox-active pyrene-4,5,9,10-tetraone (PyTE), a creation through simple Suzuki coupling conditions. PyTE-Th Polymer and TTh-Ph-PyTE CMP exhibit comparable BET surface areas and demonstrate good thermal stability, with char yields exceeding 62 wt % for each material. Electrochemical measurements reveal that TTh-Ph-PyTE CMP, featuring a triazine group with abundant heteroatoms, exhibited exceptional cycle stability of 90 % after 5000 cycles at 10 A g^{-1} and a specific capacitance of 1041 F g^{-1} (1 A g^{-1}). Notably, TTh-Ph-PyTE CMP portrays the maximum specific capacitance at 1 A g^{-1} compared to PyTE-Th polymer (486 F g^{-1}) and other porous materials, suggesting a synergistic effect of redox-active units and abundant heteroatoms.

1. Introduction

Urgent energy and environmental crises, including the depletion of fossil fuels, pollution, and climate change, are ringing alarm bells worldwide. Consequently, there is a pressing need for renewable energy storage and conversion materials, along with their associated devices [1,2]. To address these challenges, energy can be stored for electric vehicles using storage systems that facilitate the utilization of both conventional and renewable energy sources, such as solar, water, wind, and waste energy [3–7]. Additionally, energy storage systems need to meet the criteria of being environmentally sustainable, cost-effective, and high-performing, largely due to the intermittent nature of many renewable energy sources [1]. Lithium-ion batteries (LIBs) and supercapacitors (SCs) stand out as key energy storage technologies [8–10]. LIBs and SCs have gotten a lot of scrutiny as energy storage mechanisms thanks to their high energy and power densities [11]. Particularly, SCs are highly sought-after for their ability to provide high power outputs alongside suitable energy densities. Their extended cycle life and rapid charging capabilities make them valuable complements to batteries. Redox-active material-based supercapacitors (SCs) present significantly enhanced specific capacitance and energy density compared to electric double-layer capacitors (EDLCs). They not only accumulate charge at the electrical double layer but also offer pseudocapacitance generated by the reversible redox processes of electrode materials [11–13]. The overall mechanism governing the preservation of electrode materials in LIBs involves three main components: (i) the faradaic involvement gained from the Li-ion installation pathway (pseudo capacitance), (ii) the faradaic component caused by the charge-transfer activity involving atoms on the outside (pseudo capacitance), and (iii) the non-faradic aspect of the double layer effect (double layer capacitance). The former mechanism is typically associated with batteries, while the latter two mechanisms are employed in electrode materials for supercapacitors (SCs) [14–16].

The efficacy of SCs is heavily influenced by the electrode materials used [17]. A great deal of research has been put into acquiring environmentally friendly and affordably priced electrode materials for SCs [11]. Conjugated microporous polymers (CMPs) pose appealing architectures in electrochemical devices used for energy preservation and transmission, including (i) a highly accurate and flexible structure ensures sound planning and building of active sites at the atomic level and favors electrochemical phenomena and electrolytic responses at electrodes, (ii) open channels and extensive porousness may aid electrolyte permeation, conveyance of mass, and mobility of charges, increasing the permeability of a conduit may diminish hydraulic stress/strain caused by electrochemical processes, (iii) guest molecules or conductive transporters are sometimes used for enhanced electrochemical function or electricity transfer, (iv) the π-conjugated geometry supports effective charge decentralization, (v) the substantial intrinsic surface area safeguards acceptable permeable contacts connecting the electrolyte and electrode, as well as a wealth of active sites, hence strengthening electrocatalytic activity and kinetics [18].

Various materials, including carbon-based materials [19–21], metal oxides [22,23], conductive polymers [24,25], and their composites, have been extensively explored for electrode fabrication [26,27]. Within these, conductive polymers have sparked increasing scrutiny owing to their unique conjugated structures, excellent electrical conductivity, mechanical flexibility, and customizable physical properties [28]. Nevertheless, conventional conductive polymers, especially those with 1D and 2D structures, frequently encounter challenges such as low specific surface areas, pronounced pore dispersion, significant restacking, and aggregation issues. These limitations restrict ion transport, resulting in inadequate cycle life and suboptimal charge-discharge rates [29]. To overcome these limitations and achieve optimal capacitance performance, novel porous conductive polymers are being developed. Porous organic polymers, with their large specific surface areas, customizable pore topologies, fast ion diffusion capabilities, and tunable chemical activity, have emerged as promising candidates for energy storage materials. However, their low electrical conductivity has hindered their practical use in SCs [30–32]. Strategies such as composite formation [33] or carbonization [34] of porous organic polymers have been employed to enhance their specific capacitance. Unfortunately, these approaches often result in a significant reduction in the inherent benefits of porous organic polymers, limiting their potential applications. Therefore, there is a strong demand for developing and synthesizing conductive porous organic polymers tailored for supercapacitor applications. Three-dimensional conductive porous networks offer more open channels for efficient ionic transport while overcoming the limitations of low-dimensional conductive polymer materials.

Thiophene (Th), a five-membered heterocyclic molecule with one sulfur atom and four carbon atoms, is a noteworthy conductive unit that is frequently used as a building block in linear conjugated polymers. Injecting thiophene functionalities within the CMP lattice boosts the product's applicability for supercapacitor electrodes, which has various benefits. Firstly, the total electrical conductivity of CMP was impacted by the positive electron-rich π-conjugation of thiophene. Adequate electron movement across the electrode material is rendered practicable by this, which minimizes internal resistance and encourages quick charge and discharge. As a result, SCs using CMPs modified with thiophene as electrodes have improved power densities, which makes them particularly attractive for applications requiring rapid energy transfer. Further, the thiophene structure's sulfur atoms promote redox reactions, which enable the material to go through reversible faradaic processes while being stored in charge [35]. Moreover, SCs based on redox-active materials convey far greater specific capacitance and energy density than EDLCs. Additionally, they generate pseudocapacitance employing the electrode materials' reversible redox processes [36]. When contrasted with conventional inorganic electrodes such as carbons and metal oxides, redox-active polymers excel in terms of their remarkable mechanical flexibility and straightforward processing [37]. These polymers boast diverse active functionalities comprising lightweight and cost-effective elements like C, O, N, and S in their molecular compositions, facilitating redox processes for pseudocapacitance augmentation [38]. This advantage becomes particularly evident when comparing them to carbon electrode materials, which often have limited active sites. Consequently, redox polymers offer significantly greater capacitance than carbon-based compounds. One such nitrogen-rich compound, triazine units has been produced to serve as supercapacitor electrode materials. Furthermore, triazine units containing nitrogen

atoms can form redox-active sites in CMPs. To enhance the conductivity and supercapacitance of CMP-based electrodes, CMPs, and conductive moiety have been combined or composited to serve as supercapacitor electrode materials [39].

The PyTE molecule is also a prevalent organic molecule featuring carbonyl groups. It exhibits a symmetrical conjugated structure and four carbonyl functional groups, which can ensure electrochemical stability amid redox processes and translate to an excellent specific capacity [40]. Based on the information above and to understand the effect of the presence of thienyltriazine unit in organic electrode materials for energy storage. Utilizing Suzuki coupling processes, we successfully synthesized PyTE-Th polymer lacking thienyltriazine group and TTh-Ph-PyTE CMP materials with thiophene and thienyltriazine units, leveraging the PyTE unit as the primary redox-active component for both materials. Mixing 2,5-Th-2B(OH)$_2$ with brominated PyTE yielded PyTE-Th polymer, appearing as a black solid. Subsequently, combining 1,4-Ph-2B(OH)$_2$ and TTh-Br$_3$ with brominated PyTE resulted in the creation of TTh-Ph-PyTE CMP, tailored specifically for supercapacitor applications. In electrochemical assessments, TTh-Ph-PyTE CMP, distinguished by a triazine group rich in heteroatoms, exhibited remarkable cycle stability. Maintaining 90 % of its capacity at 10 A g^{-1} after 5000 cycles, it amounted to a capacitance of 1041 F g^{-1} at 1 A g^{-1}. Additionally, a symmetric supercapacitor configuration disclosed a tremendous specific capacitance of 242 F g^{-1} at 1 A g^{-1}, retaining 93 % of its capacity after 5000 cycles. The present article delves into the incorporation of thiophene's conductive nature with nitrogen-rich triazine and redox-active pyrene-4,5,9,10-tetraone, which is produced as TTh-Ph-PyTE CMP, proved worthwhile in obtaining SCs with large capacities and good cyclic stability.

2. Experimental section

2.1. Materials

Potassium carbonate (K_2CO_3), sodium bicarbonate ($NaHCO_3$), ammonum hydroxide (NH_4OH), sulfuric acid (H_2SO_4), trifluoromethanesulfonic acid (TfOH), palladium tetrakis(triphenylphosphine) [Pd(PPh$_3$)$_4$], N-bromosuccinimide (NBS), 2,5-thiophenediylbisboronic acid (2,5-Th-2B(OH)$_2$), 1,4-phenylenediboronic acid (1,4-Ph-2B(OH)$_2$) and thiophene-2-carbonitrile (Th-2CN) were among the commercially acquired materials from Sigma-Aldrich. The supporting information file included the preparation procedures for synthesizing TTh and PyTE, along with their respective FTIR and NMR analyses [Scheme S1(a) and Figs. S1, S2, S3, S6, S7, and S8].

2.2. Synthesis of 2,4,6-tris(5-bromothiophen-2-yl)-1,3,5-triazine (TTh-Br$_3$)

An excess amount of N-bromosuccinimide (NBS) (714 mg, 4 mmol) was dropped into a swirling solution of TTh (327 mg, 1 mmol) in dry $CHCl_3$ (15 mL). The resultant system was agitated for 24 h at room temperature, and then liquid bromine (640 mg, 4 mmol) was drop-by-drop introduced into the mixture. After stirring for another 24 h, the entirety was flushed with a saturated solution of $NaHCO_3$, and the organic portion was aired over anhydrous sodium sulfate (Na_2SO_4) and concentrated under reduced pressure. Afterward, the base product was purified using ethanol and $CHCl_3$ to afford a white solid (508 mg, Yield: 90 %, Scheme S1(b)). FTIR: 1507 and 1370 cm^{-1} (triazine unit). ^{1}H NMR (Fig. S4): 7.94 and 7.16 ppm (Th rings). ^{13}C NMR (Fig. S5): 167.52 (triazine moiety), 143-117 ppm.

2.3. Synthesis of PyTE-Br$_2$

PyTE (4 g, 15.2 mmol) was transferred to a chilled Schlenk flask, followed by 100 mL of concentrated H_2SO_4, and NBS (6 g, 34 mmol) was placed in the flask, and the resulting mixture was stirred for 5 h at 50 °C. PyTE-Br$_2$ was isolated as a yellow solid by extracting the resultant powder by purification in DMSO and cleaning with DCM and ether (1.26 g, 68 %, Scheme S2). FTIR (cm^{-1}, Fig. S9): 3070, 1680 (C=O). ^{1}H NMR (DMSO-d_6, 500 MHz, Fig. S10): δ = 8.4 (4H). ^{13}C NMR data of PyTE-Br$_2$ is not furnished as it is not very soluble in DMSO-d_6, and ^{13}C NMR data of PyTE-Br$_2$ is not provided.

2.4. Synthesis of PyTE-Th polymer

In the Schlenk flask, PyTE-Br$_2$ (0.5 g, 1.2 mmol), 2,5-Th-2B(OH)$_2$ (0.2 g, 1.2 mmol), K_2CO_3 (1 g, 6 mmol), and Pd (PPh$_3$)$_4$ (69 mg), DMF (24 mL), and water (6 mL) were used for polymerization to afford PyTE-Th Polymer as a black powder [0.3 g, 60 %]. M_n = 3500 g/mol.

2.5. Synthesis of TTh-Ph-PyTE CMP

In the Schlenk flask, TTh-Br$_3$ (0.25 g, 0.44 mmol), 1,4-Ph-2B(OH)$_2$ (0.11 g, 0.66 mmol), PyTE-Br$_2$ (0.28 g, 0.66 mmol), K_2CO_3 (1 g, 6 mmol), and Pd (PPh$_3$)$_4$ (69 mg), DMF (24 mL), and water (6 mL) were used for polymerization to afford TTh-Ph-PyTE CMP as a brown solid [0.13 g, 52 %].

3. Results and discussion

Scheme S1(a) depicts the initial synthesis of TTh through the utilization of TfOH within a nitrogen atmosphere. Additionally, Scheme S1 (b) outlines the production process of TTh-Br$_3$, a tribromo derivative of TTh, which was synthesized for seven days at 25 °C in the presence of a mixture of NBS/Br$_2$ as a bromination reagent in the $CHCl_3$. As illustrated in Scheme S2, the PyTE [41] underwent a reaction with a NBS in the solution of concentrated H_2SO_4, yielding PyTE-Br$_2$ as a yellow solid with high yield and purity. The spectroscopic data of TTh, TTh-Br$_3$, PyTE, and PyTE-Br$_2$ are shown in Figs. S1–S10. In this study, PyTE-Th Polymer, appearing as a black solid, and TTh-Ph-PyTE CMP, presented as a yellow powder, were synthesized via Suzuki coupling reactions. Specifically, 2,5-Th-2B(OH)$_2$/brominated PyTE and brominated PyTE/TTh-Br$_3$/1,4-Ph-2B(OH)$_2$ were reacted in a mixture of DMF/H_2O when Pd serves as a catalyst, as illustrated in Fig. 1(a). The FTIR spectrum of PyTE-Th Polymer (Fig. S11) reveals several characteristic absorption bands. The band at 1256 cm^{-1} coincides with the C-H stretching in the thiophene ring, while the band at 1396 cm^{-1} is credited to C=C's stretched peak. Additionally, the C-S symmetric and asymmetric stretching vibrations are recognized by two bands, which are spotted at 1033 cm^{-1} and 696 cm^{-1}, respectively. The peak at 1664 cm^{-1} represents the C=O functional group for the PyTE unit. In the event of TTh-Ph-PyTE CMP, the absorption maxima developed around 797 cm^{-1} corresponds to the C$_\beta$-H out-of-plane bending vibration of thiophene moiety. Additionally, the peak at 1044 cm^{-1} represents the in-plane bending vibration of C$_\beta$-H in triazine and thiophene groups. The skeletal vibration of C=C and C=N in aromatic compounds is responsible for four distinctive peaks observed at approximately 1365–1606 cm^{-1}, indicating the.

Abundance of aromatic compounds [42,43]. Furthermore, the peak at 1684 cm^{-1} could be traced to C=O groups for PyTE moieties in the TTh-Ph-PyTE CMP framework. In both solid-state ^{13}C NMR spectra (Fig. 1(b)), the signals corresponding to carbon are observed around 178.64 ppm for both PyTE-Th Polymer and TTh-Ph-PyTE CMP, attributed to the existence of the C=O group. Additionally, peaks in the range of 141.3–129.70 ppm and 150.74–126.83 ppm for PyTE-Th Polymer and TTh-Ph-PyTE CMP, respectively, indicate the aromatic rings in their skeletal structures. The thermal stability of both PyTE-Th Polymer and TTh-Ph-PyTE CMP was evaluated through thermogravimetric analysis (TGA), noting the temperatures of 5% and 10% weight loss (T_{d5} and T_{d10}) and the char yield data (Fig. 1(c)). PyTE-Th Polymer exhibited T_{d5}, T_{d10}, and char yield values of 257 °C, 332 °C, and 61 wt%, respectively. In contrast, TTh-Ph-PyTE CMP displayed superior thermal resistance and higher char yield, with T_{d5}, T_{d10}, and char yield amounts of 445 °C,

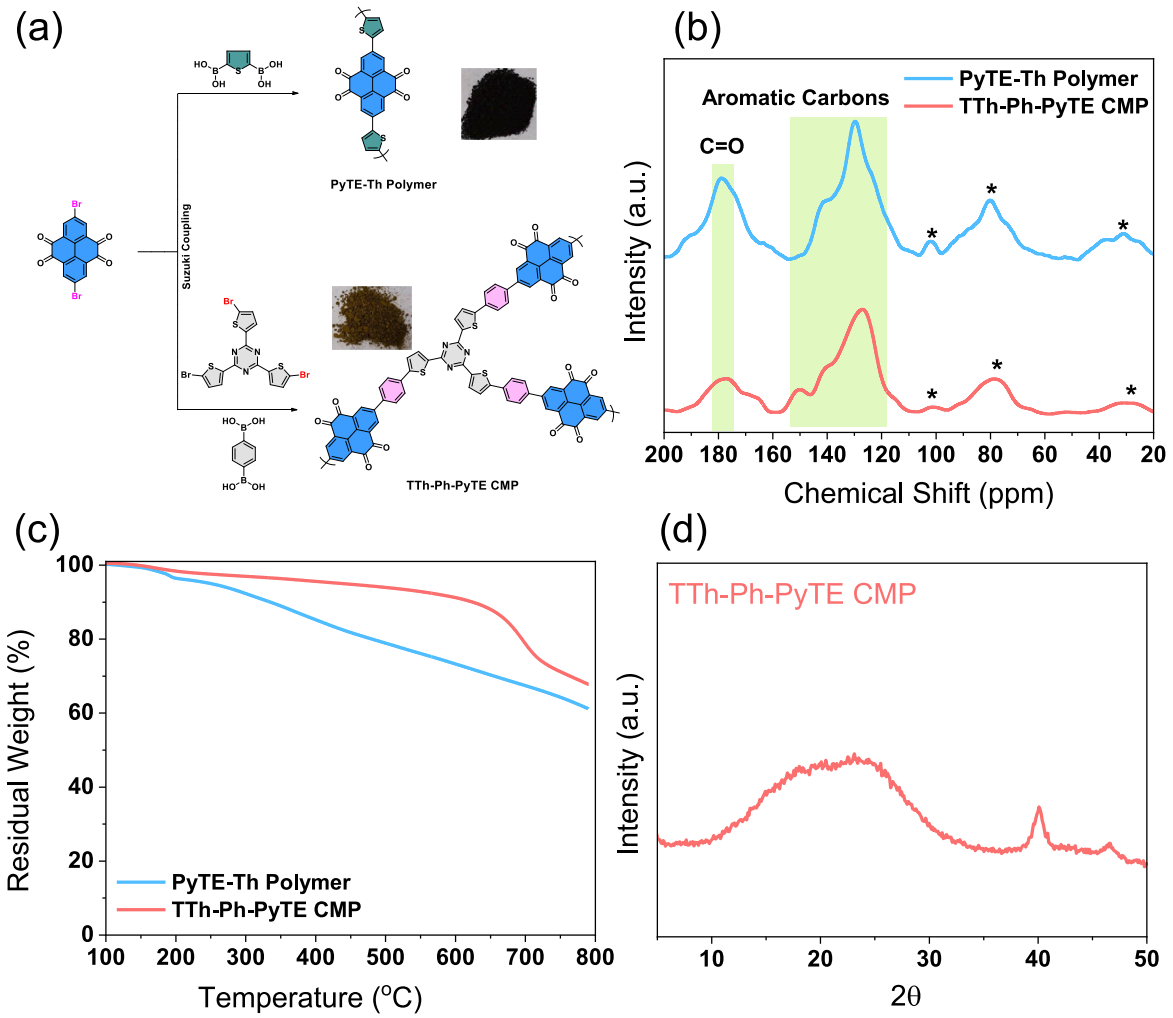

Fig. 1. (a) Preparation of PyTE-Th Polymer and TTh-Ph-PyTE CMP. (b) Solid-state ^{13}C CP/MAS NMR and (c) TGA of PyTE-Th Polymer and TTh-Ph-PyTE CMP and (d) XRD profile of TTh-Ph-PyTE CMP.

620 °C, and 67 wt%, respectively. Table S1 offers an overview of the T_{d5}, T_{d10}, and char yield numbers for the synthesized materials. These findings demonstrate that the thermal resilience of TTh-Ph-PyTE CMP improved with the incorporation of thienyltriazine and Py-ET moieties. Powder X-ray diffraction (PXRD) analysis showed that PyTE-Th Polymer and TTh-Ph-PyTE CMP had an amorphous state [Fig. 1(d) and Fig. S12]. Fig. S13 illustrates the water contact angle (WCA) of PyTE-Th Polymer and TTh-Ph-PyTE CMP. Despite both synthesized compounds exhibiting contact angles of less than 90°, indicating a hydrophilic nature in 1 M KOH electrolyte, the TTh-Ph-PyTE CMP thin film demonstrates greater hydrophilicity, with a contact angle of 23.2°, whereas the PyTE-Th Polymer exhibits a higher contact angle of 38.8°. XPS measurements were made as presented in Fig. 2(a–h). Three distinguishing elements C, O, N, and S can be spotted in PyTE-Th Polymer and TTh-Ph-PyTE CMP based on the XPS peak regions of the binding energies shown by their respective survey data [Fig. 2(a) and (d)]. According to Fig. 2(b), the peaks in the C1s spectra at 283.67, 285.09, 286.02, and 286.86 eV align with the C=C, C-C, C–S, and C=O atoms, respectively, in the PyTE-Th Polymer. The C=O atom on the PyTE unit is depicted by the peak with a binding energy of 531.17 eV [Fig. 2(c)]. The XPS high-resolution spectroscopy of TTh-Ph-PyTE CMP is displayed in Fig. 2(d). The distinct peaks of C1s [Fig. 2(e)] at 286.70 eV, 285.74 eV, 285.51 eV, 285.11 eV, and 283.82 eV are associated with, respectively, C=O atoms in PyTE unit, the sp^2 C–N in triazine groups, the sp_2 C–S in thiophene rings, the C-C atoms, and the sp_2 C=C in thiophene rings. The sp^2 C–S in thiophene rings is indicated by the splitting peaks of S2p, which include $S2p_{1/2}$ and $S2p_{3/2}$, about 164.15 and 163.06 eV respectively [Fig. 2(f)] [44], The peak with a binding energy of 531.70 eV on the PyTE unit represents the C=O atom similar to the PyTE-Th Polymer [Fig. 2(g)]. While the N1s peak signifies the N atom in the triazine unit at 397.53 eV [Fig. 2(h)] [42]. Also, the wide area under the peak for the C=O and the intensive S2p peaks in the TTh-Ph-PyTE CMP in comparison to the PyTE-Th Polymer helps us to judge that the TTh-Ph-PyTE CMP unit indeed has more C=O and S active sites. All of the aforementioned findings demonstrated that the Suzuki coupling polymerization procedure may be used to effectively construct PyTE-Th Polymer and TTh-Ph-PyTE CMP.

The pore structure analysis of TTh-Ph-PyTE CMP in this study was conducted using the Brunauer-Emmett-Teller (BET) model during nitrogen isotherm adsorption-desorption at 77.3 K. As depicted in Fig. 3 (a), the adsorption-desorption curves reveal a type II isotherm. TTh-Ph-PyTE CMP exhibited a specific surface area of 55 $m^2\ g^{-1}$.

Additionally, the overall pore volume and variations in pore size of TTh-Ph-PyTE CMP were calculated using nonlocal density functional theory (NLDFT), which were discovered to be 2.06 nm and 2.68 nm [Fig. 3(b)] and 0.15 $cm^3\ g^{-1}$, respectively. SEM studies revealed that PyTE-Th Polymer formed aggregated clusters of nanospheres (Fig. 3(c) and (d)), while TTh-Ph-PyTE CMP exhibited hairy-surfaced urchin-like spheres (Fig. 3(e) and (f)). Implementing energy dispersive spectroscopy (EDS), elemental mapping disclosed the availability of carbon (C),

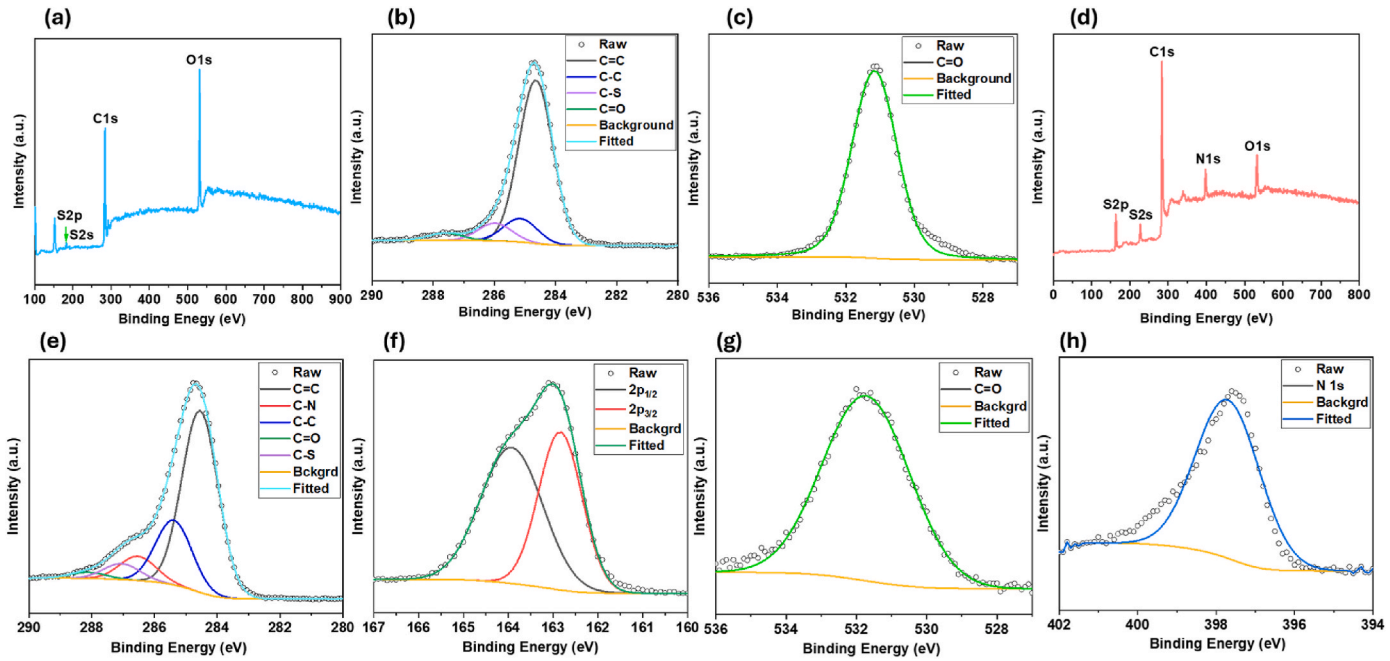

Fig. 2. (a, d) XPS survey and (b, c, e, f, g, h) XPS fitting data of (a–c) PyTE-Th Polymer and (d–h) TTh-Ph-PyTE CMP.

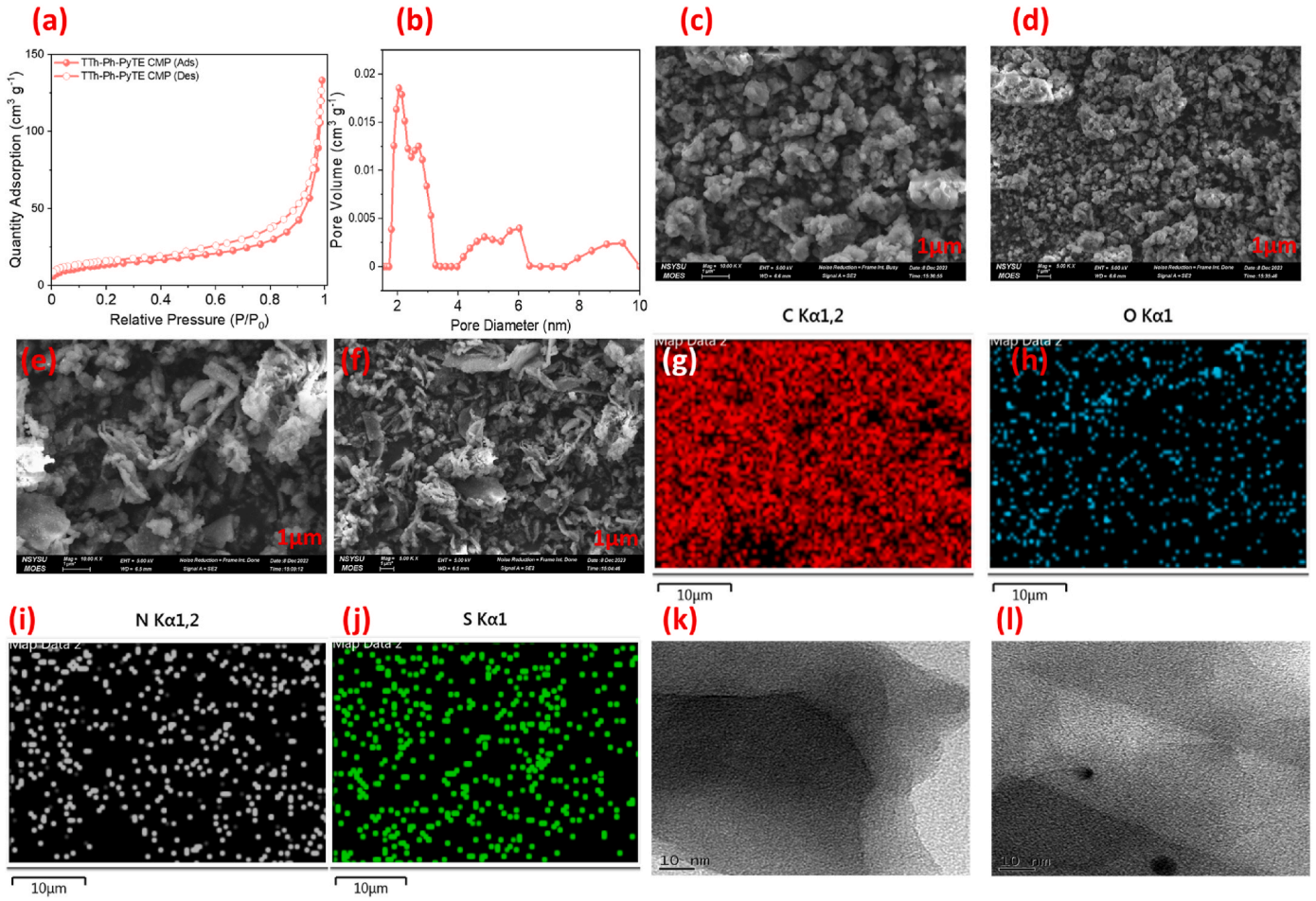

Fig. 3. (a) BET and (b) pore size profiles of TTh-Ph-PyTE CMP. (c–f) SEM images of PyTE-Th Polymer (c, d) and (e, f) TTh-Ph-PyTE CMP. SEM-EDS mapping for C (g), O (h), (N (i), and S (j) elements in the TTh-Ph-PyTE CMP framework. (k, l) TEM images of PyTE-Th Polymer (k) and TTh-Ph-PyTE CMP (l).

oxygen (O), sulfur (S), and nitrogen (N) atoms in all regions of the TTh-Ph-PyTE CMP (Fig. 3(g-j)). The HR-TEM images depicted in Fig. 3(k) and (l) further indicated that both PyTE-Th Polymer and TTh-Ph-PyTE CMP are porous and lack long-range ordering. Moreover, a small black dot observed in the TEM image of TTh-Ph-PyTE CMP [Fig. 3(l)] corresponds to the presence of Pd particles in the material.

3.1. Electrochemical performance of PyTE-Th polymer and TTh-Ph-PyTE CMP in three-electrodes system

The electrochemical performance of engineered materials, PyTE-Th Polymer and TTh-Ph-PyTE CMP was evaluated in a 1M KOH aqueous solution using cyclic voltammetry (CV) and galvanostatic charge-discharge (GCD) profiles. A three-electrode arrangement namely, glassy carbon, Hg/HgO, and platinum wire was employed, with the working, reference, and counter electrodes, respectively. Fig. 4(a) and (b) illustrate the CV curves of both the synthesized PyTE-Th Polymer and TTh-Ph-PyTE CMP across several different scan rates (5–200 mV s^{-1}) within a potential range of −1.0 to 0.0 V. The CV curves had a peculiar quasi-rectangular form with a humped portion that denoted capacitance from dependable current sweeps and electric double-layer capacitors (EDLC). Both redox and EDLC processes have an impact on the supercapacitor's capacity for storing. Two pairs of redox peaks relative to Hg/HgO were seen in the CVs of PyTE-Th Polymer and TTh-Ph-PyTE CMP. This illustrates how important redox reactions are to the behavior of the material. An electrode's overall capacitance can be divided into its component portions. One is the speedy faradaic reaction of oxidation and reduction entities and a swift electrochemical process that entails ion adsorption and desorption. The remainder is regulated by the dispersal of ions in the electrolyte and electrode content. A CV profile of both PyTE-Th Polymer and TTh-Ph-PyTE CMP can also be used to illustrate the kinetics of the material's energy storage mechanism. Additionally, at multiple current density levels that cover from 1 to 15 A g^{-1}, the compounds' capacitance and charge/discharge curves were examined [Fig. 4(c) and (d)]. The EDLC and pseudo-capacitive properties of the GCD curves were shown by their triangular form and mild bend. For each compound, the discharge time was greater periods than the charge time, which suggested greater capacitance. Low scan rates led to higher capacitance, considering that the electrolyte's ions may reach the majority of the charged components' active sites. On the other hand, lesser capacitance was produced by greater scan rates since they accelerated the electrolyte's access to the electroactive components [44].

The specific capacitance of PyTE-Th Polymer and TTh-Ph-PyTE CMP at 1 A g^{-1} were 468 and 1041 F g^{-1}, respectively (Fig. 5(a)). With a specific capacitance of 600 F g^{-1} for TTh-Ph-PyTE CMP versus 100 F g^{-1} for PyTE-Th Polymer at a high current density of 15 A g^{-1}, TTh-Ph-PyTE CMP demonstrated a specific capacitance that was six times greater than that of the PyTE-Th Polymer, despite a surge in current density. The specific capacitance of both compounds rapidly dropped as the current density rose. Due to the fact the electrolyte ions weren't given the opportunity for transit into the pores at higher current densities, charge storage took place primarily on the outside active surface [45]. These compounds' performance during 5000 charge/discharge cycles at a high scan rate density of 10 A g^{-1} revealed their long-term stability for

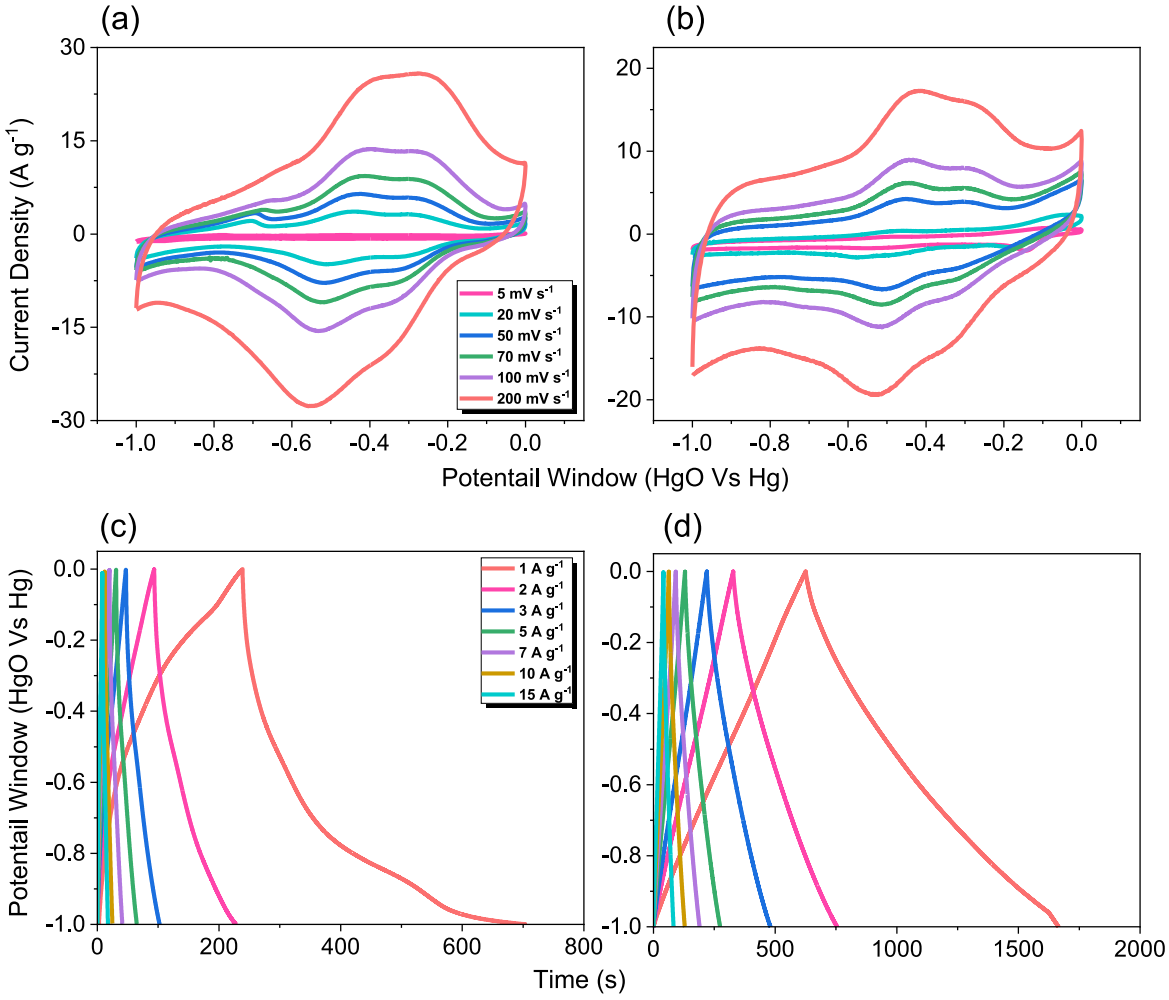

Fig. 4. (a, b) CV and (c, d) GCD profiles of PyTE-Th Polymer (a, c), and TTh-Ph-PyTE CMP (b, d).

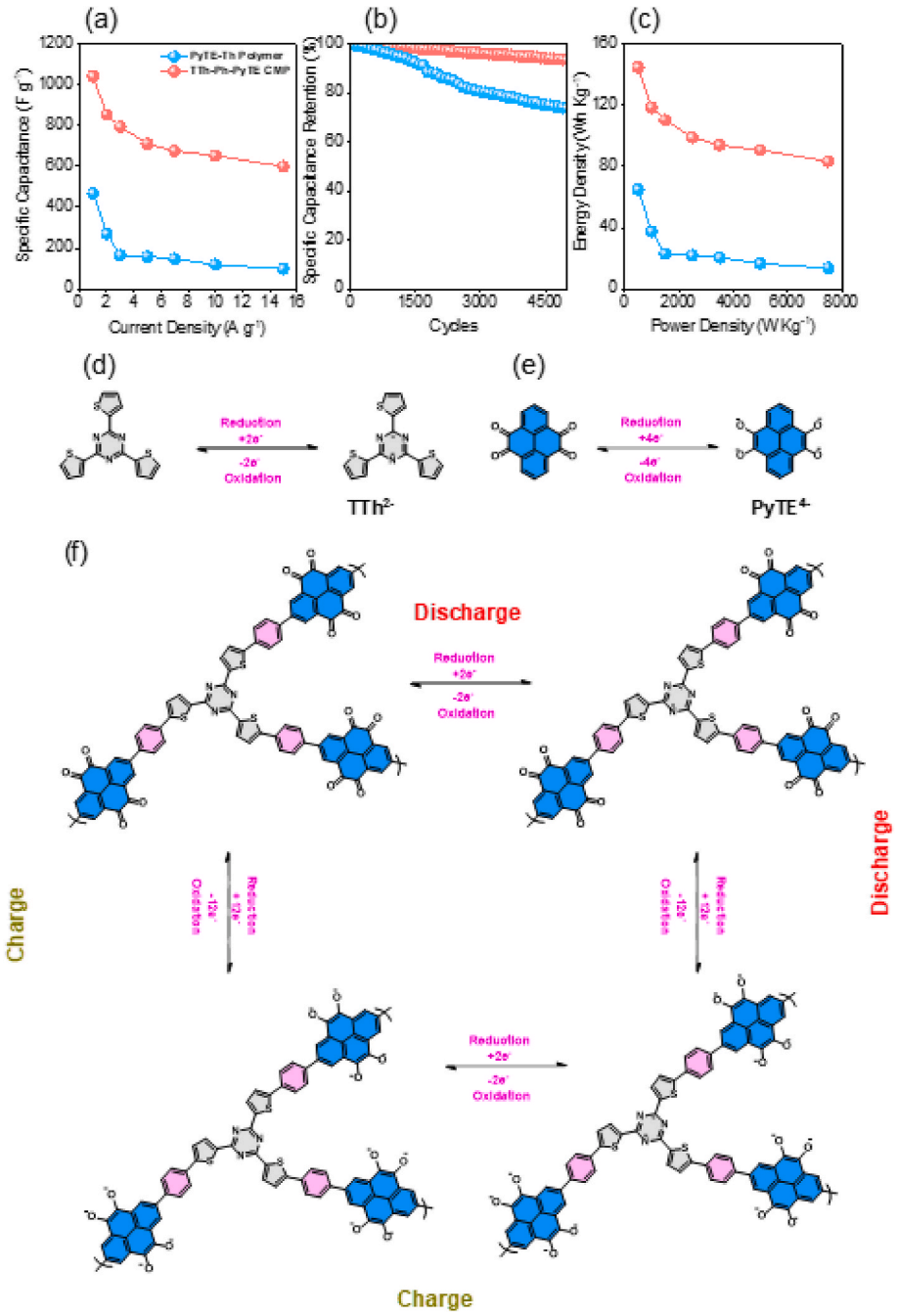

Fig. 5. Specific capacitance (a), durability (b), Ragone (c) profiles of PyTE-Th Polymer and TTh-Ph-PyTE CMP. (d–f) Suggested redox reactions of (d) TTh, (e) PyTE, and (f) TTh-Ph-PyTE CMP.

electrochemical energy storage applications. As proven in Fig. 5(b), 5000 charge/discharge cycles at an elevated scan rate density of 10 A g^{-1} were performed to assess the electrode materials' long-term durability. For TTh-Ph-PyTE CMP, 93.5 %, and 73.86 % for PyTE-Th polymer, the capacity retention throughout these cycles was calculated. According to Figs. S14 and S15, the Coulombic efficiency for the PyTE-Th polymer and TTh-Ph-PyTE CMP in three-electrode SCs was determined to be 99.7 % and 100 %, respectively. As shown in Fig. S16, after 5000 cycles, the PyTE-Th polymer and TTh-Ph-PyTE CMP exhibit aggregated formations of nanospheres and nanorods structures; respectively. Furthermore, using the Ragone plot in Fig. 5(c), it was possible to calculate the materials' energy densities. With energy density values of 144.55 Wh kg^{-1} and 65.03 W kg^{-1}, respectively, the TTh-Ph-PyTE CMP endured more than double the energy density of PyTE-Th Polymer. The TTh-Ph-PyTE material, featuring redox-active PyTE units, electron-rich phenyl rings, and incorporating nitrogen heteroatoms within the triazine moiety, displayed exceptional cycle stability attributed to the heightened conductivity facilitated by the nitrogen heteroatom present within the material [46]. The combination of the TTh and PyTE components forms the foundation for the redox mechanism observed in the TTh-Ph-PyTE CMP, as depicted in Fig. 5 (d–f). In this mechanism, two electrons are reduced into the TTh^{2-} anion [75] [Fig. 5(d)], while four electrons are reduced into the $PyTE^{4-}$ anion in the redox reaction mechanism of PyTE [47] [Fig. 5(e)]. The resulting TTh-Ph-PyTE CMP exhibits significant redox characteristics. As illustrated in [Fig. 5(f)], the structures of the TTh-Ph-PyTE CMP undergo reduction throughout the discharge process, while the TTh^{2-} and $PyTE^{4-}$ anions undergo oxidation across the entire charge state.

For more study, Cottrell's equation (I α $\nu^{0.5}$) which shows the linear relation between redox peaks current density (I) with the square root of potential scan rate ($\nu^{0.5}$) of PyTE-Th Polymer and TTh-Ph-PyTE CMP electrodes [Fig. 6(a) and (b)] [48,49], verifying that surface-bound pseudocapacitance and electric double-layer capacitance are always included in the cathodic/anionic peaks [50]. Sankar and Selvan used the approach to determine the ratios of surface-controlled capacitive and non-surface-controlled diffusion ratios to the PyTE-Th Polymer and TTh-Ph-PyTE CMP electrode's overall charge storage. Both the PyTE-Th Polymer and TTh-Ph-PyTE CMP electrode charge storage mechanisms could be investigated by the Trasatti method [51]. This technique determines the relative contribution of surface-controlled capacitive and non-surface-controlled diffusion to the total charge stored (Q_{total}) in a given material. The equation that follows was used to determine the value of the outer charge (Q_{outer}), which emerges when a potential scan rate reaches its maximum value, which is mostly a surface process as indicated in Fig. 6(c) and (e).

$$Q = Q_{outer} + K\nu^{0.5}$$

When K is a constant, ν (mV s^{-1}) communicates the potential sweep rate, and Q shows the capacity (C g^{-1}) derived from each CV at the equivalent potential sweep rate. The value of (Q_{outer}) can be computed using the intercept of the Q vs. $\nu^{-0.5}$plot. Furthermore, the longer dissemination of ions is allowed to occur at the lower the scan rate. The total charge (Q_{total}) in this case is represented by the stored charges. This can be obtained using the following equation, which is derived from the plotted intercept between ($1/Q$) and ($\nu^{0.5}$), as shown in **Fig. 6(d) and (f)** for the PyTE-Th Polymer and TTh-Ph-PyTE CMP, respectively.

$$\frac{1}{Q} = \frac{1}{Q_{total}} + K\nu^{0.5}$$

Because of the foregoing, the outer charge and total charge of the PyTE-Th Polymer and TTh-Ph-PyTE CMP electrodes are 14.3 and 25.7 C g^{-1}, and 403 and 303 C g^{-1}, respectively. Consequently, diffusion-controlled faradaic PyTE-Th Polymer yields 85.3 %, while TTh-Ph-PyTE CMP yields 48.6 %. The proportion of surface and diffusion-controlled inputs at various possible scan rates are shown in **Fig. 6(g) and (h)**.

Our TTh-Ph-PyTE CMP, as depicted in Fig. S17(a) and Table S2, demonstrated the greatest specific capacitance compared to alternative electrode precursors. The ion diffusion process was also utilized to investigate the electric resistance provided by various electrodes using electrochemical impedance spectroscopy. The distinct Nyquist plots are shown in Fig. S17(b) to compare various characteristics, including charge transfer and series, from the electrodes. The electrode/electrolyte/current collector supercapacitor system's primary resistive attribute is represented by a relatively tiny semicircle in the high-frequency band. On the Z′ axis, the resistivity (R_s) of the solution at the interface between the electrode and current collector is displayed at the left intercept of the semicircle line, and the internal resistance (R_p) of the electrode is displayed at the right intercept of the semicircle line. The

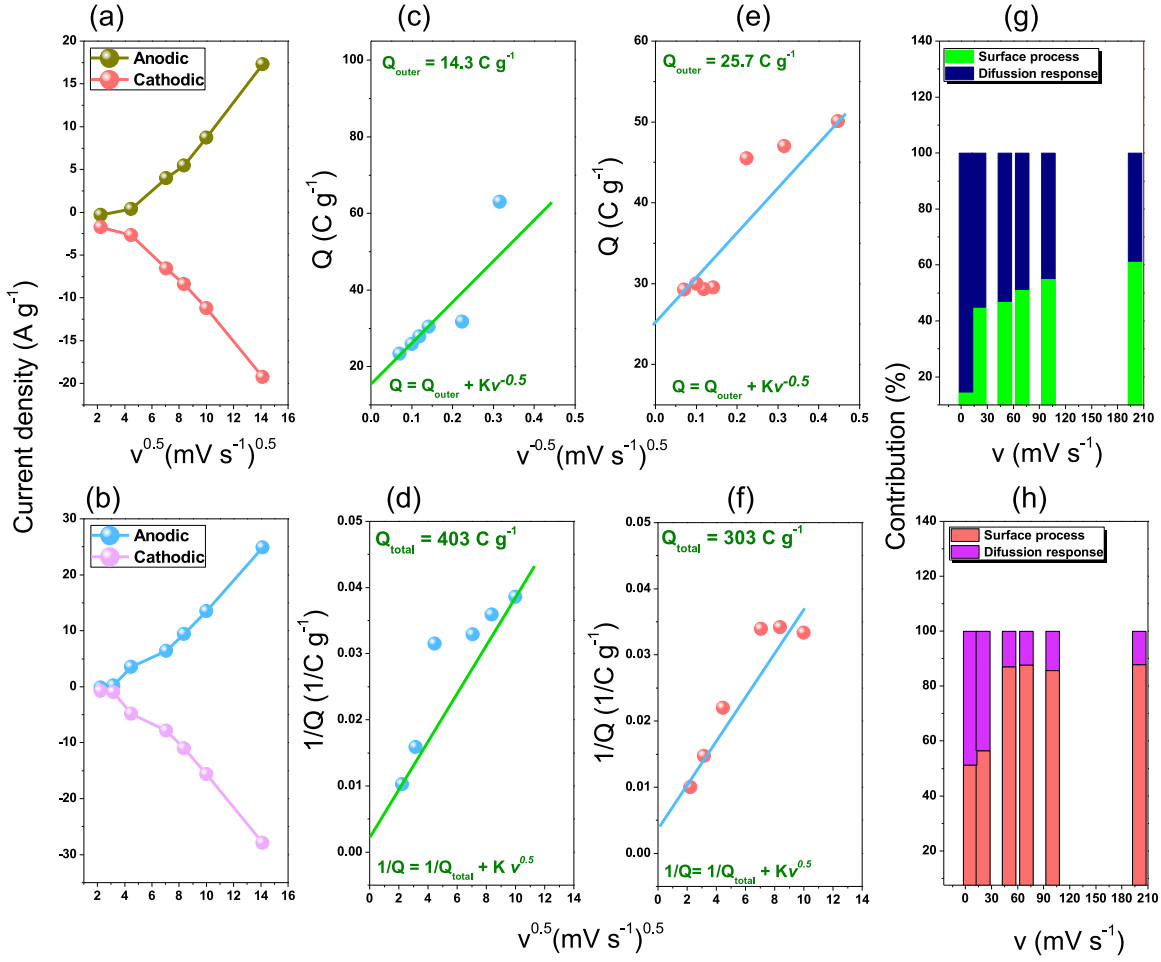

Fig. 6. The relation between peak current density and the square root of potential scan rate (a) PyTE-Th Polymer and (b) TTh-Ph-PyTE CMP. (c, e) Relation between Q (C g^{-1}) and $\nu^{-0.5}$ (mV s^{-1})$^{-0.5}$, (d, f) 1/Q vs. $\nu^{0.5}$, and (g, h) Percentage of surface contribution and diffusion-contribution for (c, d, g) PyTE-Th Polymer and (e, f, h) TTh-Ph-PyTE CMP.

semicircle's diameter (R_p-R_s) and the ESR value are the same. The stronger capacitive conduct as the outcome of electrical and ionic charge creation of the electrochemical double-layer structure across the exteriors of micropores is shown by the sharply increasing horizontal lines in the low-frequency region, where ions may more easily enter the micropores. For TTh-Ph-PyTE CMP and PyTE-Th Polymer, the starting series resistance also referred to as the ohmic resistance values, are 0.80 and 4.27 Ω, while after 5000 cycles, they were found to be 0.86 and 4.75 Ω respectively. In addition to being shorter than PyTE-Th polymer's straight line, TTh-Ph-PyTE CMP's slopes away from the vertical Z″ axis, suggesting a greater Warburg length/resistance. In the case of TTh-Ph-PyTE CMP, the thiophene content surpasses that of the synthesized PyTE-Th Polymer. Moreover, the porous structure of the TTh-Ph-PyTE CMP facilitates smooth charge flow within the material's bulk, resulting in reduced ohmic resistance. Nyquist plots depict the real and imaginary parts of impedance (Z(w)) on the X and Y axes respectively. These plots reveal distinct features: a 45° linear segment at moderate frequencies denoting molecular diffusion (the Warburg region), semicircles at high frequencies indicating faradaic redox reactions or electronic conduction of electrodes, and a 90° linear segment at low frequencies signifying the formation of a double layer on the electrode surface. Examination of the EIS [Fig. S18] of TTh-Ph-PyTE CMP at various voltages ranging from −1 to 0 V demonstrates a tail on the plot increasingly angled towards the y-axis as voltage sweeps from −1 to 0. This inclination suggests heightened molecular diffusion at higher voltages, underscoring the effectiveness of our synthesized TTh-Ph-PyTE CMP under such conditions. Fig. S19 shows a graph between sheet resistance and resistance. The resistance along with sheet resistance, sheet resistance, conductivity of TTh-Ph-PyTE CMP (2.6 x 10^3 Ω/sq) is less than PyTE-Th Polymer (2.27 x10^3 Ω/sq). The conductivity value of TTH-Ph-PyTE CMP (3.85 x 10^2 Siemen/cm) is higher than TTH-Ph-PyTE CMP (4.40 x 10^1 Siemen/cm).

3.2. *Constructing a symmetric supercapacitor coin cell for TTh-Ph-PyTE CMP*

Apart from evaluating the three-electrode performance of these developed products, we also constructed symmetric coin cell supercapacitors as an aspect of our research on the real utilization of TTh-Ph-PyTE CMP. The coin cell was constructed using the CR2032 coin cell, which has an anode and cathode, a separator, a bottom and top cover, and an electrolyte. With TTh-Ph-PyTE CMP serving as the cathode and anode, we constructed a symmetric supercapacitor. The suspension originated by applying the proportion specified by the manuscript and then pouring over carbon paper. An aqueous 1.0 M KOH electrolyte was used with a Selemion AMV membrane. Every electrochemical experiment was carried out across multiple scan rates, differing from 5 to 200 mV s^{-1}, and between potentials of −0.3 and 0.2 V. Fig. 7(a) sets forth the CV analysis of symmetric coin cells for supercapacitor computed at scan speeds of 5–200 mV s^{-1}. These CV curves have an entirely rectangular form due to the integrated action of the electric double-layer capacitor (EDLC) and the pseudocapacitive concerning the electrode substance. The increased durability and the rate of these electrode materials were made apparent with an upsurge in current density once we lifted the

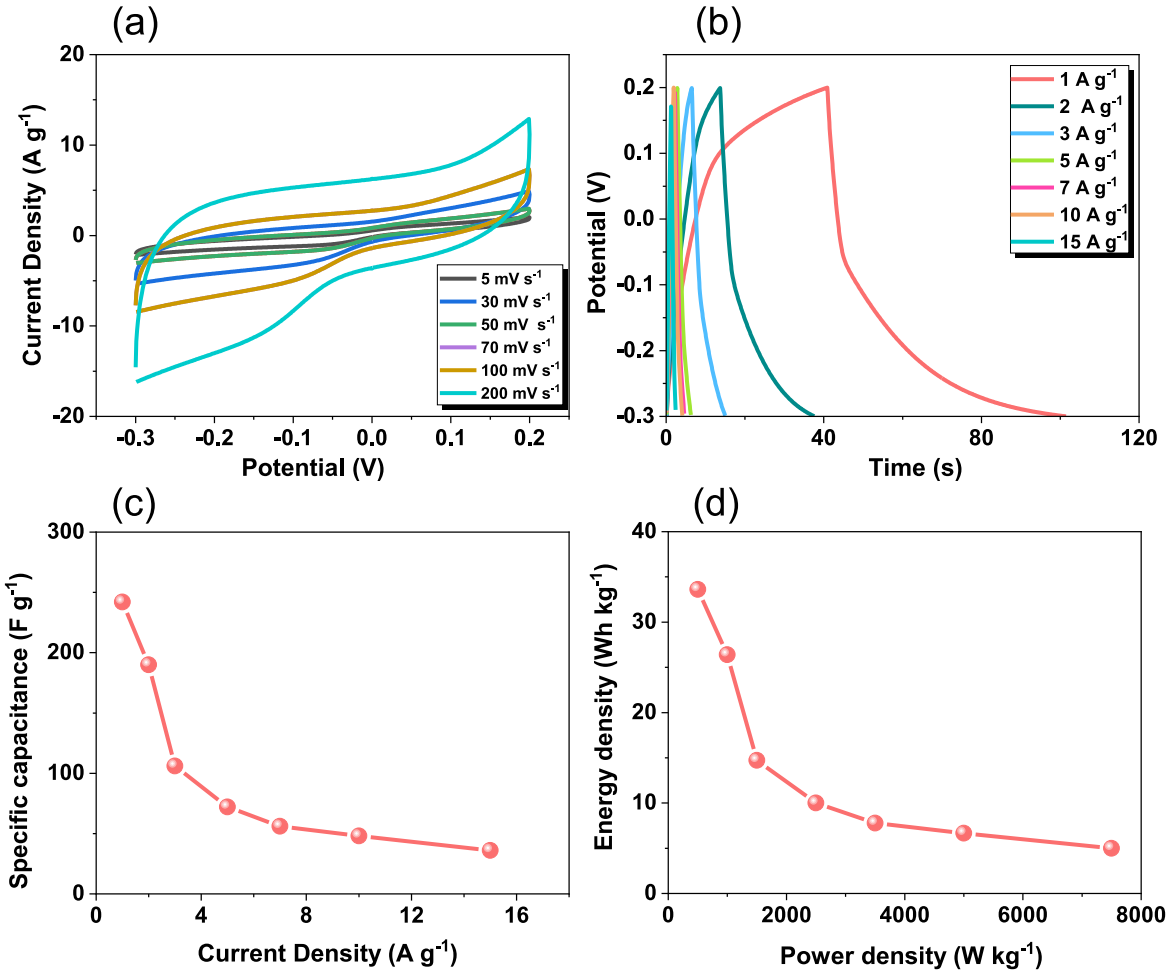

Fig. 7. CV (a), GCD (b), specific capacitance (c), Ragone (d) profiles for symmetric supercapacitor coin cell of TTh-Ph-PyTE CMP.

scan speeds from 5 to 200 mV s^{-1}. Furthermore, we assessed the TTh-Ph-PyTE CMP electrodes' performance using GCD tests, that were conducted at current densities varying from 1 to 15 A g^{-1} (Fig. 7(b)). The GCD curves featured triangle shapes with a little bend that alluded to EDLC characteristics and pseudo capacity. This curve's discharge time is typically connected with the specific capacitance. For a current density of 1 A g^{-1}, the TTh-Ph-PyTE CMP electrode [Fig. 7(c)] conveyed a formidable specific capacitance of 242 F g^{-1} at 1 A g^{-1}, with retention rates of 93 % following 5000 cycles (set at 10 A g^{-1}) [Fig. S20]. The coulombic efficiency of the symmetric device using TTh-Ph-PyTE CMP was found to be 100 %. [Fig. S21]. The comparison of the capacitance has been included in the supporting information (Table S3) which shows that the produced symmetric device outshines some of the reported materials. Including heteroatoms, which promote capacity retention and enhance the link between the electrode and electrolyte, is responsible for this improved durability. In terms of energy densities, we discovered that, as Fig. 7(d) illustrates the TTh-Ph-PyTE CMP had an energy density of 35 W h kg^{-1} at a power density of 7540 W kg^{-1}, which is comparatively higher than some of the alternative materials (Table S3).

Meanwhile, the ion diffusion process served to investigate the electric resistance stipulated by various electrodes via electrochemical impedance spectroscopy. In Fig. 8, several Nyquist plots are shown alongside similar fitted circuits to compare multiple features that involve charge transfer and series from the electrodes. The equivalent series resistance, charge transfer resistance, constant phase elements (which reflect the pseudocapacitive and EDLC behaviors), and Warburg element are embodied by the symbols R_s, R_{ct}, CPE-P, CPE-EDL, and Z_w in the fitted circuit, respectively. Table S4 discloses that the electrode's initial series resistance, sometimes referred to as its Ohmic resistance value, was 3.93 Ω. Furthermore, TTh-Ph-PyTE CMP has R_{ct} value of 12.8 Ω. In addition, the Bode plot of the frequency-dependent amplitude is visible in Fig. S22(a). The results show tiny resistances at high frequencies and slant lines with a negative slope at low frequencies, indicating the electrode materials' exceptional capacitive properties. Conversely, the frequency-dependent phase angle graphs of multiple electrodes are displayed in Fig. S22(b). Based on this illustration, the knee frequencies were assessed at a phase angle of −45°, the moment whereby the electrodes' capacitive and resistive qualities are equivalent. TTh-Ph-PyTE CMP's knee frequencies were 16.76 Hz, in that order. The rate of performance is directly correlated with knee frequency. According to reports, enhanced rate performance is often associated with increased knee frequency. The supercapacitor becomes increasingly resistive above the knee frequency, which is also the point at which the porous network structure's electrolyte ion diffusion begins [52,53].

Fig. S23 illustrates the frontier molecular orbitals of both PyTE-Th Polymer and TTh-Ph-PyTE CMP. The extent of delocalization in molecular orbital distribution significantly influences the electrochemical characteristics of these polymers. Both PyTE-Th Polymer and TTh-Ph-PyTE CMP exhibit substantial delocalization, with molecular orbitals spread widely across their conjugation backbones. Interestingly, despite having comparable energy levels, there is a noticeable performance gap between the electrochemical properties of PyTE-Th Polymer and TTh-Ph-PyTE CMP. The TTh-Ph-PyTE CMP notably outperforms PyTE-Th Polymer in supercapacitor performance. The molecular electrostatic potential (MESP) images [Fig. S24] provided offer insights into this performance difference. The TTh-Ph-PyTE CMP displays a greater number of active sites compared to PyTE-Th Polymer, indicating enhanced electrochemical reactivity. Additionally, the incorporation of the triazine unit in TTh-Ph-PyTE CMP is anticipated to further augment its electrochemical behavior. Consequently, with its increased active sites and unique molecular structure, TTh-Ph-PyTE CMP is poised to exhibit superior electrochemical performance.

4. Conclusion

Utilizing basic Suzuki coupling procedures, PyTE/TTh-based materials were successfully synthesized, featuring redox-active units and heteroatoms. Their impact on supercapacitor performance as electrode materials was thoroughly investigated. The synthesized TTh-Ph-PyTE CMP exhibited notable porosity and thermal stability. Electrochemical property analysis revealed both normal ELDC and pseudocapacitance behavior, along with high capacitance and excellent cycle stability over 5000 cycles. TTh-Ph-PyTE CMP showcased the highest capacitance, reaching 1041 F g^{-1} at 1 A g^{-1} with 93.41 % capacity retention after 5000 cycles. Moreover, TTh-Ph-PyTE CMP exhibited a remarkable specific capacity of 242 F g^{-1} at 1 A g^{-1} with 93 % capacity preservation after 5000 cycles when employed as a symmetric supercapacitor. The excellent output can be correlated to the presence of heteroatoms, which facilitated charge delocalization, improved wettability, and electrostatic coupling. These findings underscore the importance of investigating redox-type materials for SC applications.

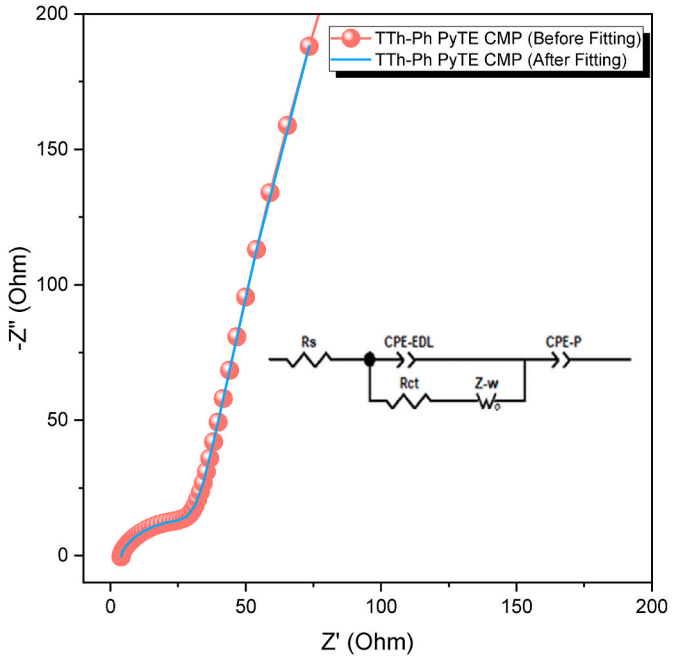

Fig. 8. Nyquist plots for symmetric supercapacitor coin cell of TTh-Ph-PyTE CMP. Inset in Fig. 8: the fitting equivalent circuit for a two-electrode system.

CRediT authorship contribution statement

Swetha V. Chaganti: Writing – original draft, Investigation. **Santosh U. Sharma:** Investigation, Conceptualization. **Mervat Ibrahim:** Methodology, Investigation. **Abdul Basit:** Investigation. **Poonam Nagendra Singh:** Investigation. **Shiao-Wei Kuo:** Supervision. **Mohamed Gamal Mohamed:** Writing – review & editing, Writing – original draft, Supervision, Methodology, Investigation, Data curation, Conceptualization.

Declaration of competing interest

The authors declare that they have no known competing financial interests or personal relationships that could have appeared to influence the work reported in this paper.

Acknowledgments

This study was supported financially by the National Science and Technology Council, Taiwan, under contracts NSTC 112-2218-E-110-007, and 112-2223-E-110-004. The authors thank the staff at National Sun Yat-sen University for their assistance with the TEM (ID:

EM022600) experiments.

Appendix A. Supplementary data

Supplementary data to this article can be found online at https://doi.org/10.1016/j.jpowsour.2024.235848.

Data availability

The data that has been used is confidential.

References

[1] N. Mahmood, C. Zhang, H. Yin, Y. Hou, Graphene-based nanocomposites for energy storage and conversion in lithium batteries, supercapacitors and fuel cells, J. Mater. Chem. A 2 (2014) 15–32, https://doi.org/10.1039/C3TA13033A.

[2] Y. Sun, Q. Wu, G. Shi, Graphene based new energy materials, Energy Environ. Sci. 4 (2011) 1113–1132, https://doi.org/10.1039/C0EE00683A.

[3] M.G. Mohamed, S.U. Sharma, C.H. Yang, M.M. Samy, A.A.K. Mohammed, S. V. Chaganti, J.T. Lee, S.W. Kuo, Anthraquinone-enriched conjugated microporous polymers as organic cathode materials for high-performance lithium-ion batteries, ACS Appl. Energy Mater. 4 (2021) 14628–14639, https://doi.org/10.1021/acsaem.1c03270.

[4] M.G. Mohamed, C.C. Chen, M. Ibrahim, A.O. Mousa, M.H. Elsayed, Y. Ye, S.W. Kuo, Tetraphenylanthraquinone and Dihydroxybenzene-Tethered conjugated microporous polymer for enhanced CO_2 uptake and supercapacitive energy storage, JACS Au (2024), https://doi.org/10.1021/jacsau.4c00537.

[5] J. Hou, Z. Liu, P. Zhang, A new method for fabrication of graphene/polyaniline nanocomplex modified microbial fuel cell anodes, J. Power Sources 224 (2013) 139–144, https://doi.org/10.1016/j.jpowsour.2012.09.091.

[6] E.H. Yu, X. Wang, U. Krewer, L. Li, K. Scott, Direct oxidation alkaline fuel cells: from materials to systems, Energy Environ. Sci. 5 (2012) 5668–5680, https://doi.org/10.1039/C2EE02552C.

[7] C. Zhang, R. Hao, H. Yin, F. Liu, Y. Hou, Iron phthalocyanine and nitrogen-doped graphene composite as a novel non-precious catalyst for the oxygen reduction reaction, Nanoscale 4 (2012) 7326–7329, https://doi.org/10.1039/C2NR32612D.

[8] M.G. Fayed, S.Y. Attia, Y.F. Barakat, E.E. El-Shereafy, M.M. Rashad, S.G. Mohamed, Carbon and nitrogen co-doped MoS_2 nanoflakes as an electrode material for lithium-ion batteries and supercapacitors, Sustain. Mater. Technol. 29 (2021) e00306, https://doi.org/10.1016/j.susmat.2021.e00306.

[9] S. Mekhilef, R. Saidur, A. Safari, A review on solar energy use in industries, Renew. Sustain. Energy Rev. 15 (2011) 1777–1790, https://doi.org/10.1016/j.rser.2010.12.018.

[10] M.G. Mohamed, M.M. Samy, T.H. Mansoure, C.J. Li, W.C. Li, J.H. Chen, K. Zhang, S.W. Kuo, Microporous carbon and carbon/metal composite materials derived from bio-benzoxazine-linked precursor for CO_2 capture and energy storage applications, Int. J. Mol. Sci. 23 (2022) 347, https://doi.org/10.3390/ijms23010347.

[11] A.K. Mondal, D. Su, S. Chen, A. Ung, H.S. Kim, G. Wang, Mesoporous $MnCo_2O_4$ with a flake-like structure as advanced electrode materials for lithium-ion batteries and supercapacitors, Chem. Eur J. 21 (2015) 1526–1532, https://doi.org/10.1002/chem.201405698.

[12] C. Mu, J. Fang, J. Nie, L. Fu, W. Li, Embedding hydrogel electrodes into hydrogel Electrolyte: an 3D protecting strategy for stretchable High-Performance supercapacitor, Chem. Eng. J. 484 (2024) 149505, https://doi.org/10.1016/j.cej.2024.149505.

[13] H. Pan, X. Jiao, W. Zhang, L. Fan, Z. Yuan, C. Zhang, Supercapacitor with Ultra-High power and energy density enabled by Nitrogen/Oxygen-Doped interconnected hollow carbon Nano-Onions, Chem. Eng. J. (2024) 149663, https://doi.org/10.1016/j.cej.2024.149663.

[14] J. Niu, R. Shao, J. Liang, M. Dou, Z. Li, Y. Huang, F. Wang, Biomass-derived mesopore-dominant porous carbons with large specific surface area and high defect density as high performance electrode materials for Li-ion batteries and supercapacitors, Nano Energy 36 (2017) 322–330, https://doi.org/10.1016/j.nanoen.2017.04.042.

[15] B.E. Conway, V. Birss, J. Wojtowicz, The role and utilization of pseudocapacitance for energy storage by supercapacitors, J. Power Sources 66 (1997) 1–14, https://doi.org/10.1016/S0378-7753(96)02474-3.

[16] Q. Wang, J. Yan, Z. Fan, Carbon materials for high volumetric performance supercapacitors: design, progress, challenges and opportunities, Energy Environ. Sci. 9 (2016) 729–762, https://doi.org/10.1039/C5EE03109E.

[17] A.K. Mondal, D. Su, S. Chen, K. Kretschmer, X. Xie, H.J. Ahn, G. Wang, A microwave synthesis of mesoporous $NiCo_2O_4$ nanosheets as electrode materials for lithium-ion batteries and supercapacitors, ChemPhysChem 16 (2015) 169–175, https://doi.org/10.1002/cphc.201402654.

[18] B. Zhang, W. Wang, L. Liang, Z. Xu, X. Li, S. Qiao, Prevailing conjugated porous polymers for electrochemical energy storage and conversion: lithium-ion batteries, supercapacitors and water-splitting, Coord. Chem. Rev. 436 (2021) 213782, https://doi.org/10.1016/j.ccr.2021.213782.

[19] D. Zhu, K. Cheng, Y. Wang, D. Sun, L. Gan, T. Chen, J. Jiang, M. Liu, Nitrogen-doped porous carbons with nanofiber-like structure derived from poly (aniline-co-p-phenylenediamine) for supercapacitors, Electrochim. Acta 224 (2017) 17–24, https://doi.org/10.1016/j.electacta.2016.12.023.

[20] Q. Ma, Y. Yu, M. Sindoro, A.G. Fane, R. Wang, H. Zhang, Carbon-based functional materials derived from waste for water remediation and energy storage, Adv. Mater. 29 (2017) 1605361, https://doi.org/10.1002/adma.201605361.

[21] D. Xu, W. Hu, X.N. Sun, P. Cui, X.Y. Chen, Redox additives of Na_2MoO_4 and KI: synergistic effect and the improved capacitive performances for carbon-based supercapacitors, J. Power Sources 341 (2017) 448–456, https://doi.org/10.1016/j.jpowsour.2016.12.031.

[22] F. Chen, X. Liu, Z. Zhang, N. Zhang, A. Pan, S. Liang, R. Ma, Controllable fabrication of urchin-like Co_3O_4 hollow spheres for high-performance supercapacitors and lithium-ion batteries, Dalton Trans. 45 (2016) 15155–15161, https://doi.org/10.1039/C6DT02603F.

[23] D.P. Dubal, N.R. Chodankar, R. Holze, D.H. Kim, P. Gomez-Romero, Ultrathin mesoporous $RuCo_2O_4$ nanoflakes: an advanced electrode for high-performance asymmetric supercapacitors, ChemSusChem 10 (2017) 1771–1782, https://doi.org/10.1002/cssc.201700001.

[24] Y. Ma, C. Hou, H. Zhang, M. Qiao, Y. Chen, H. Zhang, Q. Zhang, Z. Guo, Morphology-dependent electrochemical supercapacitors in multi-dimensional polyaniline nanostructures, J. Mater. Chem. A 5 (2017) 14041–14052, https://doi.org/10.1039/C7TA03279J.

[25] Y. Huang, H. Li, Z. Wang, M. Zhu, Z. Pei, Q. Xue, Y. Huang, C. Zhi, Nanostructured polypyrrole as a flexible electrode material of supercapacitor, Nano Energy 22 (2016) 422–438, https://doi.org/10.1016/j.nanoen.2016.02.047.

[26] A. Borenstein, O. Hanna, R. Attias, S. Luski, T. Brousse, D. Aurbach, Carbon-based composite materials for supercapacitor electrodes: a review, J. Mater. Chem. A 5 (2017) 12653–12672, https://doi.org/10.1039/C7TA00863E.

[27] M. Tong, S. Liu, X. Zhang, T. Wu, H. Zhang, G. Wang, Y. Zhang, X. Zhu, H. Zhao, Two-dimensional CoNi nanoparticles@ S, N-doped carbon composites derived from S, N-containing Co/Ni MOFs for high performance supercapacitors, J. Mater. Chem. A 5 (2017) 9873–9881, https://doi.org/10.1039/C7TA01008G.

[28] A. Afzal, F.A. Abuilaiwi, A. Habib, M. Awais, S.B. Waje, M.A. Atieh, Polypyrrole/carbon nanotube supercapacitors: technological advances and challenges, J. Power Sources 352 (2017) 174–186, https://doi.org/10.1016/j.jpowsour.2017.03.128.

[29] G.A. Snook, P. Kao, A.S. Best, Conducting-polymer-based supercapacitor devices and electrodes, J. Power Sources 196 (2011) 1–12, https://doi.org/10.1016/j.jpowsour.2010.06.084.

[30] J. Huang, C. Liu, Y. Jin, J. Chen, Hierarchical porous carbon synthesis by carbonized polymer dots-based sacrificial template for high-performance supercapacitors, Chem. Eng. J. 461 (2023) 141930, https://doi.org/10.1016/j.cej.2023.141930.

[31] P.N. Singh, M.G. Mohamed, S.-W. Kuo, Systematic design and synthesis of conjugated microporous polymers containing pyrene and azobenzene building materials for high-performance energy storage, ACS Appl. Energy Mater. 6 (2023) 11342–11351, https://doi.org/10.1021/acsaem.3c02252.

[32] A.O. Mousa, M.G. Mohamed, C.-H. Chuang, S.-W. Kuo, Carbonized aminal-linked porous organic polymers containing pyrene and triazine units for gas uptake and energy storage, Polymers 15 (2023) 1891, https://doi.org/10.3390/polym15081891.

[33] B. Sun, J. Liu, A. Cao, W. Song, D. Wang, Interfacial synthesis of ordered and stable covalent organic frameworks on amino-functionalized carbon nanotubes with enhanced electrochemical performance, Chem. Commun. 53 (2017) 6303–6306, https://doi.org/10.1039/C7CC01902E.

[34] C. Zhang, R. Kong, X. Wang, Y. Xu, F. Wang, W. Ren, Y. Wang, F. Su, J.X. Jiang, Porous carbons derived from hypercrosslinked porous polymers for gas adsorption and energy storage, Carbon 114 (2017) 608–618, https://doi.org/10.1016/j.carbon.2016.12.064.

[35] S.U. Sharma, M.H. Elsayed, I.M.A. Mekhemer, T.S. Meng, H.H. Chou, S.W. Kuo, M. G. Mohamed, Rational design of pyrene and thienyltriazine-based conjugated microporous polymers for high-performance energy storage and visible-light photocatalytic hydrogen evolution from water, Giant 17 (2024) 100217, https://doi.org/10.1016/j.giant.2023.100217.

[36] B. Esser, F. Dolhem, M. Becuwe, P. Poizot, A. Vlad, D. Brandell, A perspective on organic electrode materials and technologies for next generation batteries, J. Power Sources 482 (2021) 228814, https://doi.org/10.1016/j.jpowsour.2020.228814.

[37] L. Dominique, J.M. Tarascon, Towards greener and more sustainable batteries for electrical energy storage, Nat. Chem. 7 (2015) 19–29, https://doi.org/10.1038/nchem.2085.

[38] W. Yaqun, Y. Ding, L. Pan, Y. Shi, Z. Yue, Y. Shi, G. Yu, Understanding the size-dependent sodium storage properties of $Na_2C_6O_6$-based organic electrodes for sodium-ion batteries, Nano Lett. 16 (2016) 3329–3334, https://doi.org/10.1021/acs.nanolett.6b00954.

[39] N.R. Kumar, P. Das, A.R. Agrawal, S.K. Mandal, S.S. Zade, Thienyltriazine based conjugated porous organic polymers: tuning of the porosity and band gap, and CO_2 capture, Mater. Adv. 2 (2021) 7473–7481, https://doi.org/10.1039/D1MA00621E.

[40] M. Shi, C. Peng, X. Zhang, A novel aqueous asymmetric supercapacitor based on pyrene-4,5,9,10-tetraone functionalized graphene as the cathode and annealed $Ti_3C_2T_x$ MXene as the anode, Small 19 (2023) 2301449, https://doi.org/10.1002/smll.202301449.

[41] M.G. Mohamed, S.V. Chaganti, S.U. Sharma, M.M. Samy, M. Ejaz, J.T. Lee, K. Zhang, S.W. Kuo, Constructing conjugated microporous polymers containing the pyrene-4,5,9,10-tetraone unit for energy storage, ACS Appl. Energy Mater. 5 (2022) 10130–10140, https://doi.org/10.1021/acsaem.2c01842.

[42] D. Lörchner, D. Dittmann, U. Braun, L.W. Kroh, R. Köppen, Investigation of two triazine-based heterocyclic brominated flame retardants by coupled

thermogravimetry-Fourier transform infrared spectroscopy, J. Anal. Appl. Pyrolysis 141 (2019) 104635, https://doi.org/10.1016/j.jaap.2019.104635.
[43] X. Xue, J. Luo, L. Kong, J. Zhao, Y. Zhang, H. Du, S. Chen, Y. Xie, The synthesis of triazine–thiophene–thiophene conjugated porous polymers and their composites with carbon as anode materials in lithium-ion batteries, RSC Adv. 11 (2021) 10688–10698, https://doi.org/10.1039/D0RA10862F.
[44] X. Guo, Q. Yuan, C. Li, H. Du, J. Zhao, L. Liu, Y. Li, Y. Xie, V. Vaidya, The synthesis of alternating donor–acceptor polymers based on pyrene-4,5,9,10-tetraone and thiophene derivatives, their composites with carbon, and their lithium storage performances as anode materials, RSC Adv. 11 (2021) 15044–15053, https://doi.org/10.1039/D1RA00794G.
[45] M.M. Samy, M.G. Mohamed, S.W. Kuo, Pyrene-functionalized tetraphenylethylene polybenzoxazine for dispersing single-walled carbon nanotubes and energy storage, Compos. Sci. Technol. 199 (2020) 108360, https://doi.org/10.1016/j.compscitech.2020.108360.
[46] M.M. Samy, M.G. Mohamed, A.F.M. EL-Mahdy, T.H. Mansoure, K.C.W. Wu, S. W. Kuo, High-performance supercapacitor electrodes prepared from dispersions of tetrabenzonaphthalene-based conjugated microporous polymers and carbon nanotubes, ACS Appl. Mater. Interfaces 13 (2021) 51906–51916, https://doi.org/10.1021/acsami.1c05720.
[47] V.V. Kondratiev, R. Holze, Intrinsically conducting polymers and their combinations with redox-active molecules for rechargeable battery electrodes: an update, Chem. Pap. 75 (2021) 4981–5007, https://doi.org/10.1007/s11696-021-01529-7.
[48] K.V. Sankar, R.K. Selvan, The ternary $MnFe_2O_4$/graphene/polyaniline hybrid composite as negative electrode for supercapacitors, J. Power Sources 275 (2015) 399–407, https://doi.org/10.1016/j.jpowsour.2014.10.183.
[49] Y. Jiang, C. Tang, H. Zhang, T. Shen, C. Zhang, S. Liu, Hierarchical walnut-like $Ni_{0.5}$ $Co_{0.5}O$ hollow nanospheres comprising ultra-thin nanosheets for advanced energy storage devices, J. Mater. Chem. A 5 (2017) 5781–5790, https://doi.org/10.1039/C6TA10730C.
[50] Y. Tao, L. Zaijun, L. Ruiyi, N. Qi, K. Hui, N. Yulian, L. Junkang, Nickel–cobalt double hydroxides microspheres with hollow interior and hedgehog-like exterior structures for supercapacitors, J. Mater. Chem. 22 (2012) 23587, https://doi.org/10.1039/c2jm35263j.
[51] T.T. Nguyen, D. Mohapatra, D.R. Kumar, M. Baynosa, S. Sahoo, J. Lee, J.J. Shim, Direct growth of nickel cobalt layered double hydroxide on nickel foam via redox reaction between nitrate ion and ethanol for hybrid supercapacitors, Electrochim. Acta 367 (2021) 137226, https://doi.org/10.1016/j.electacta.2020.137226.
[52] Z. Weng, Y. Su, D.W. Wang, F. Li, J. Du, H.M. Cheng, Graphene–cellulose paper flexible supercapacitors, Adv. Energy Mater. 5 (2011) 917–922, https://doi.org/10.1002/aenm.201100312.
[53] R. Xu, F. Guo, X. Cui, L. Zhang, K. Wang, J. Wei, High performance carbon nanotube based fiber-shaped supercapacitors using redox additives of polypyrrole and hydroquinone, J. Mater. Chem. A . 44 (2015), https://doi.org/10.1039/C5TA06165B, 22353-22360, 10.